Dynamics Analysis for DC Transformers iIntegration in Hybrid AC-DC Power Distribution Networks

J. Mace, R. Barcelos, M. Dupont, *et al.*

IET Power Electronics

ORIGINAL RESEARCH

Dynamics analysis for DC transformers integration in hybrid AC-DC power distribution networks

Jules Mace [iD] | **Renan Pillon Barcelos** | **Max Dupont** | **Andrea Cervone** [iD] | **Drazen Dujic**

Power Electronics Laboratory, Ecole Polytechnique Federale de Lausanne (EPFL), Lausanne, Switzerland

Correspondence
Jules Mace, Power Electronics Laboratory, Ecole Polytechnique Federale de Lausanne (EPFL), 1015 Lausanne, Switzerland.
Email: jules.mace@epfl.ch

Funding information
H2020 European Research Council, Grant/Award Number: 957788

Abstract

In AC/DC power distributions networks, power converters are interfacing buses to ensure DC voltage regulation and power distribution. Active front ends are used between AC and DC buses and two typical control schemes that can be implemented are voltage regulation or power regulation. On the DC side, open-loop operated DC transformers could be used between two DC buses to provide voltage adaptation, isolation and natural power flow. In this context, power flows and DC bus voltages in the power distribution network are dependent on the combined operation of the active front ends and the DC transformer. Mainly studied from a stability perspective, this interdependency between active front ends and DC transformers has lacked investigations in terms of dynamics. Fast dynamics is nevertheless important to operate optimally a network. In this paper, the assessment of the dynamic performance for distribution systems with DC transformers is performed for different mixes of voltage regulating and power regulating active front ends. The influence of DC line length and DC transformer power reversal method on the system is further investigated. A model of the system is proposed, validated experimentally and can be used to aid system level design and analysis of future DC systems.

1 | INTRODUCTION

Hybrid AC/DC distributions systems have gained popularity with the development of DC microgrids and the necessity to interface AC and DC subgrids of different voltage levels [1, 2]. This interfacing is done by power converters that offer several benefits compared to conventional AC transformers such as power flows and voltage levels control [3] and reduced size [4]. To interface an AC node with a DC node, active front ends (AFEs) are employed, converters that can regulate AC power or DC bus voltage to enable power flow control and voltage regulation for the DC power distribution network (PDN).

In order to provide voltage adaptation and galvanic isolation between the AC networks, AC transformers are employed. In DC networks, the DC transformer (DCT) concept has emerged as its equivalent in a DC system. Galvanically DC/DC isolated converters [5] are employed to provide voltage adaptation and a similar behavior as AC transformers. A lot of development has been done around DCTs: new topologies with modular designs [6], development of high power bulk power processing

converters with high power semiconductor switches [7], multi-port converters [8, 9] and energy routers [10–12]. Converters can be controlled in closed-loop, typically with topologies such as Dual Active Bridge (DAB) [13], or in open-loop, using resonant topologies. The benefit of resonant topologies such as the LLC converter [5] is that they do not require active regulation to offer transformer-like capabilities: natural and bidirectional power flow. One actively controlled device can then ensure power and voltage regulation across all connected DC buses while being both galvanically isolated from each other and with potentially different voltage levels. This approach significantly reduces the power flow control of DC grids [14, 15]. Extensive research has been performed to model, design and improve resonant converters [16], and enhance power factor or voltage gain characteristic [17].

In an AC/DC distribution system with AFEs and DCTssuch as the one in Figure 1, the AFE can be used as a power source (e.g. as done in [4] to investigate the DCT design) or as a voltage source (e.g. as done in [18] to investigate the impact of the DCT on the system stability, when AFEs are regulating the voltage).
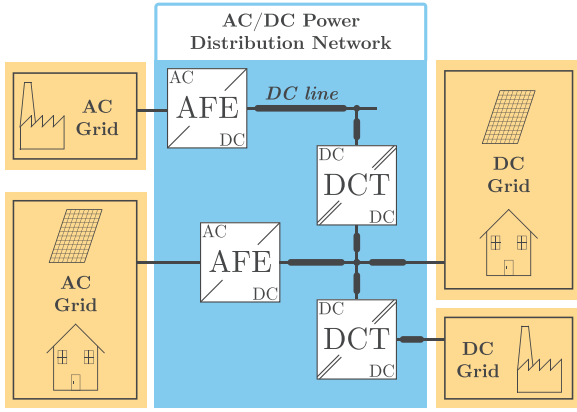
FIGURE 1 Example of a hybrid AC/DC power distribution network with DC transformers interconnecting DC buses.

Indeed, inserting a DCT between DC lines connected to AFEs introduces an additional element that naturally has an impact on the system dynamics and overall performance. Interaction between AFEs and DCTs has been investigated in two different aspects: the power flow control coordination between DCTs and AFEs [4, 17] (for optimal utilization of the DCT) and the stability issue [18]. It is also important to address this interaction from a dynamics perspective, as a fast response leads to better power flow control. The small-signal model of an AFE derived in [19] can be used to investigate the dynamic response of an AFE connected to a stiff current source and a model of DCT [17] describes also well the converter impedance and its losses. However, combined use of those two models has not been evaluated to model power and voltage transients.

Furthermore, in distribution systems, as converters can be distributed over long distances, DC transformers could be located far away from an AFE, and dynamics for remote or close DCT must be assessed, similarly to the approach taken by [18] to evaluate the stability.

The main contributions of this paper are the development of a model for a network with DCTs and the comprehensive comparison, supported by experiments, of the AFEs configurations on the power and voltage transients of an AC-DC PDN. The model is also validated experimentally for different network configurations. Furthermore, effect of the DC line length and DCT efficiency and power reversal method on the system dynamics is also evaluated, stressing the importance to take into account those parameters during grid planning or operation.

The paper is structured as follows: in Section 2, the converters (AFEs and DCTs) and other system elements (DC lines) are presented. Then, in Section 3, a PDN model based on the system elements is derived for predicting the PDN response. In Sections 4 and 5, this model is validated experimentally. In Section 6, discussions about the DCT model are provided.

2 | SYSTEM ELEMENTS

Different elements of a hybrid AC/DC power distribution network are considered in this work: active front ends, DC
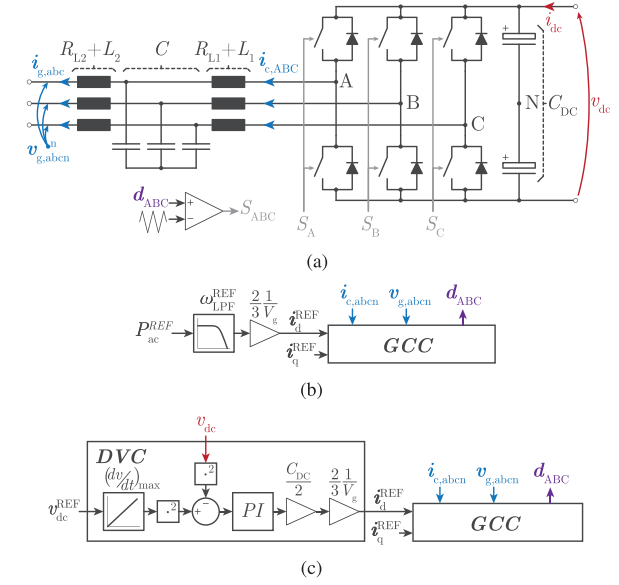
FIGURE 2 Schemes of AFEs: (a) power stage, (b) controller of a PR-AFE and (c) controller of a VR-AFE.

transformers and lines. In this section, the topologies and control schemes of each element is presented along with models that will later be used to model the overall PDN dynamic behavior.

2.1 | Active front end

The AFE, shown in Figure 2a, is employed to either regulate the AC power or the DC voltage. In the case of a power regulating AFE (PR-AFE), a single stage controller for AC currents regulation is implemented as in Figure 2b, with a phase-locked loop (PLL) ensuring grid angle tracking. Meanwhile, in the case of voltage regulating AFE (VR-AFE), the controller is extended with a second stage, regulating the DC voltage by adjusting the AC power reference. As shown in Figure 2c, a PI-based voltage controller is implemented.

The VR-AFE controller transfer function would, when the dynamics of the AC side grid current control are ignored, be written as:

$$T_{\text{dvc}}(s) = \frac{i_{\text{dc,AFE}}}{v_{\text{dc}}^{\text{REF}} - v_{\text{dc}}} = C_{\text{DC}} \cdot \frac{K_{\text{P,DVC}}s + K_{\text{I,DVC}}}{s}. \quad (1)$$

The PR-AFE current transfer function can be modeled as a simple first order low-pass filter:

$$G_{\text{REF}}(s) = \frac{i_{\text{dc,AFE}}}{i_{\text{dc,AFE}}^{\text{REF}}} = \frac{\omega_{\text{gcc}}}{s + \omega_{\text{gcc}}}. \quad (2)$$

2.2 | DC transformer

The DC transformer analyzed in this paper is a bidirectional resonant converter based on the LLC topology as displayed
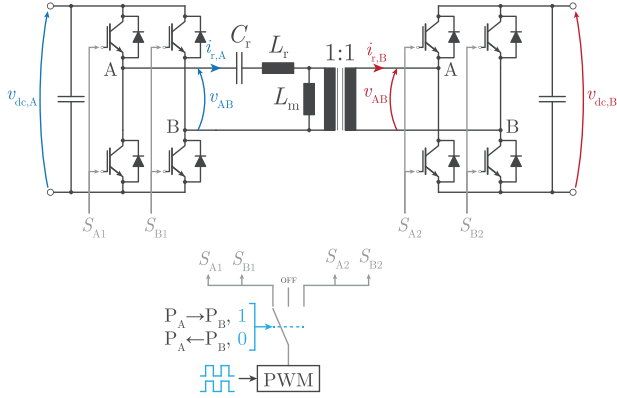
FIGURE 3 DCT scheme with the power stage (LLC topology) and the controller stage, activating one full-bridge or another depending on the power flow direction ($P_A \rightarrow P_B$ or $P_A \leftarrow P_B$).
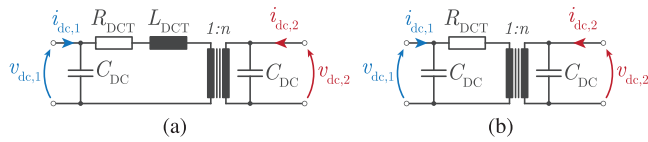
FIGURE 4 (a) Model of the DCT based on [16]. (b) Simplified model.

in Figure 3 and operating near the resonant frequency. It is operated in open-loop by modulating only the primary-side or the secondary-side full-bridge, without any active power flow regulation.

The model used in this work for the DCT is based on [16] where the model is derived to describe the behavior of DCTs during transients. The model, illustrated here in Figure 4a is using equivalent DC capacitance, resistance and inductance that can be either extracted from theoretical computation or through characterization and measurements. The DC capacitances are the DC-link capacitances of each full-bridge. The DC equivalent resistance is associated with the losses (and therefore efficiency) and is preferably small. The DC inductance is associated to the resonant tank inductance L_r. The relationships between the DC values and the physical inductance and resistance is given in [16]:

$$\begin{cases} L_{DC} = \alpha^2 \cdot L_r \\ R_{DC} = \beta^2 \cdot R_{total} \end{cases}, \quad (3)$$

where R_{total} is the DCT total series resistance.

Theoretical α and β can be computed considering piecewise sinusoidal currents [16]:

$$\begin{cases} \alpha^{TH} = \frac{\pi}{2} \cdot \frac{f_r}{f_{sw}} \\ \beta^{TH} = \frac{\pi}{2\sqrt{2}} \cdot \sqrt{\frac{f_r}{f_{sw}}} \end{cases}. \quad (4)$$

In the DCTs employed in this study, the time constant $\tau = \frac{L_{DCT}}{R_{DCT}}$ is very small (around 40 μs), the inductance can be

neglected and hence, the model can be simplified to one shown in Figure 4b.

2.3 | Modeling of the DC lines

DC lines, which can vary largely between PDNs, can be modeled conventionally with π-sections as in Figure 6 for short line lengths. In this study, the time constant of the RL section, $\tau = \frac{L_l}{R_l} = 3$ ms, is very small and hence, similarly to the DCT model, L_l can be neglected and a model with a resistor R_l and two capacitances can be considered.

3 | SYSTEM MODELING

By combining the previously presented element models, a parametric model for the PDN is obtained. Considering a simple topology as in Figure 5, where two DC buses are interconnected with one DCT, the AFEs can be set in two configurations. The two AFEs can either be set as VR-AFEs, and the power transferred between the DC lines is controlled by adjusting the DC bus voltage difference, or one AFE can be set as a PR-AFE while the second one is a VR-AFE, hence regulating simultaneously the two DC bus voltages through an open-loop DCT.

The two configurations are modeled in the following section and results are then generalized to larger PDNs with any mix of VR-AFEs and PR-AFEs.

3.1 | Modeling of the system in VR-VR configuration

This modeling is performed by combining the models of the lines, the DCT and the AFEs presented in the previous section.In a first model, considering step changes in AFE2 reference, AFE1, whose voltage reference is fixed, is modeled as an ideal voltage source, significantly reducing the complexity of the model. In a second model, the controller action of AFE1 is included in the system model, improving the accuracy of the transient prediction.

3.1.1 | Model I

Considering AFE1 as a voltage source, the PDN can be simplified to Figure 7a. The DC grid can be modeled as Figure 7b. The plant transfer function is:

$$H(s) = \frac{v_{dc}}{i_{dc,AFE}} = \frac{1}{C'_{DC} \cdot s + \frac{1}{R'_{DCT}}}$$

$$\text{with} \begin{cases} C'_{DC} = C_{DC,AFE} + C_{DC,DCT} \\ R'_{DCT} = R_{DCT} + R_{l1} + R_{l2} \end{cases}. \quad (5)$$
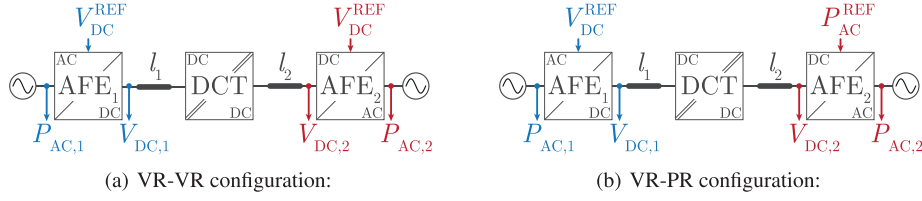
FIGURE 5 Schemes of the PDN configurations: (a) VR-VR configuration, (b) VR-PR configuration.
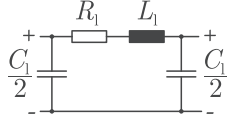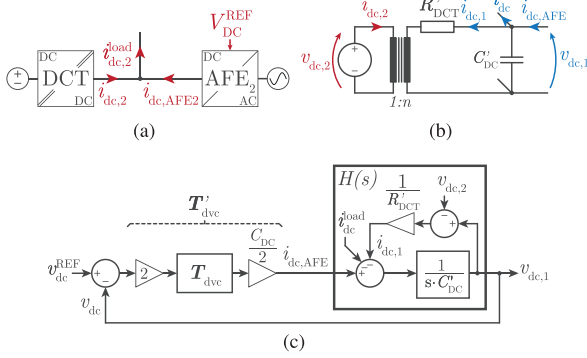

FIGURE 6 Lumped π-section model of a DC line.

FIGURE 7 Simplified DC System in VR-VR configuration (Model I): (a) system layout, (b) equivalent circuit and (c) control loop.
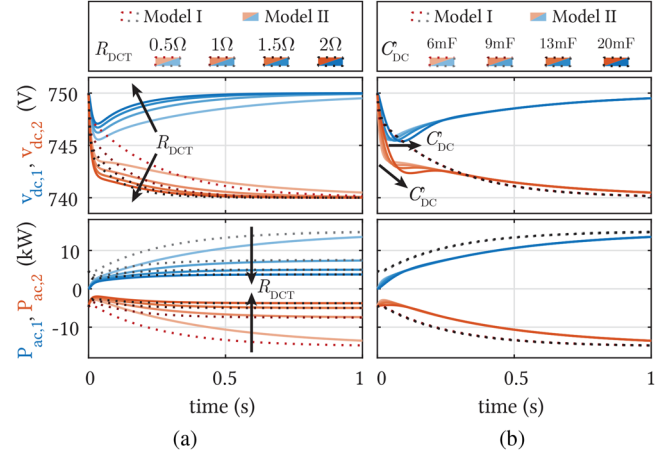

FIGURE 8 Step response to a 10 V step for different (a) DCT resistance, (b) DCT capacitances for the PDN in VR-VR configuration.

**TABLE 1** System and component nominal values.

Parameter	Value
$K_{P,DVC}$	133
$K_{I,DVC}$	2133
C'_{DCT}	6 mF
R'_{DCT}	0.4 Ω

The DC lines and the DCT hence impacts the plant model both at steady-state ($H(j0) = R'_{DCT}$) and during transients with the pole $\frac{1}{C'_{DC} \cdot R'_{DCT}}$ that varies with the resistance and capacitance.

Using the control loop outlined in Figure 7c, the DC voltage transfer function G_{dvc} becomes then:

$$G_{dvc}(s) = \frac{v_{dc}}{v_{dc}^{REF}} = \left(1 + H \cdot T'_{dvc}\right)^{-1} \cdot H \cdot T'_{dvc}$$

$$= \frac{K_{P,DVC} \cdot s + K_{I,DVC}}{\dfrac{C'_{DC}}{C_{DC,AFE}} s^2 + \left(K_{P,DVC} + \dfrac{1}{R'_{DCT} \cdot C_{DC,AFE}}\right) s + K_{I,DVC}} . \quad (6)$$

And the voltage to power transfer function $G_{P,Vdc}$ is:

$$G_{Vdc,P}(s) = \frac{P_{ac}}{v_{dc}^{REF}} = V_{DC} \cdot T'_{dvc} \cdot (1 - G_{dvc})$$

$$= \frac{V_{DC} \cdot C_{DC,AFE} \left(K_{P,DVC} \cdot s + K_{I,DVC}\right) \left(C'_{DC} \cdot s + \dfrac{1}{R'_{DCT}}\right)}{\dfrac{C'_{DC}}{C_{DC,AFE}} s^2 + \left(K_{P,DVC} + \dfrac{1}{R'_{DCT} C_{DC,AFE}}\right) s + K_{I,DVC}} . \quad (7)$$

Together, G_{dvc} and $G_{Vdc,P}$ are modeling, respectively, the voltage and power responses to a voltage reference step in AFE2, with simple second order transfer functions. In Figure 8, step responses are modeled for a PDN with parameters values defined as in Table 1 and for different DCT resistances and DC capacitances. As in (6) and (7), the DCT resistance mainly acts on the damping factor. This can be well observed in Figure 8a, where the step response is damped more when the resistance decreases. The DC capacitance C'_{DC} on the other hand is having very little impact on the response as it affects both the damping ratio and natural frequency, hence limiting its effect on the high frequency pole of the system as observed in Figure 8b.

3.1.2 | Model II

If the AFE1 is included in the model, a second model including the two AFEs and their controllers can also be derived. The scheme, circuit and control loop are presented in Figure 9.
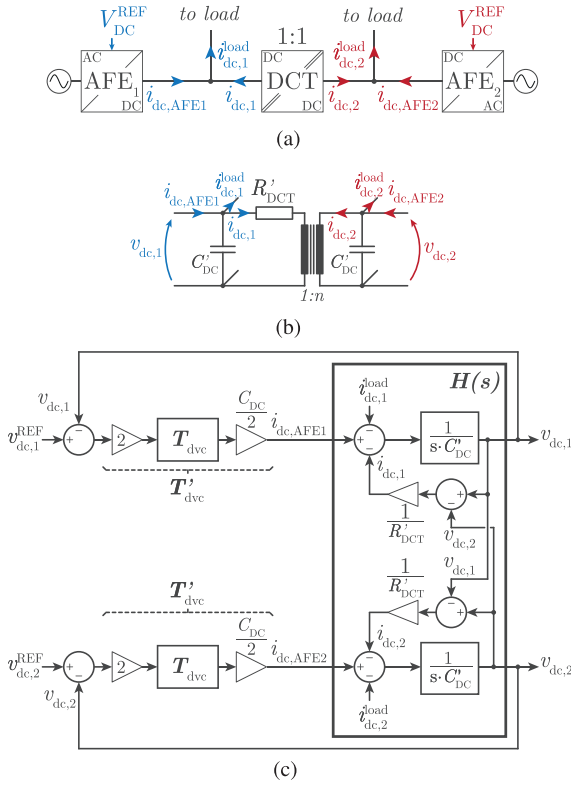
FIGURE 9 Simplified DC System in VR-VR configuration (Model II): (a) system layout, (b) equivalent circuit and (c) control loop.

Based on Figure 9b, the plant equations can be written as:

$$\underbrace{\begin{bmatrix} v_{dc,1} \\ v_{dc,2} \end{bmatrix}}_{v_{dc}} = \underbrace{\left(C's + R'^{-1}_{DCT} \right)^{-1}}_{H(s)} \cdot \underbrace{\begin{bmatrix} i_{AFE,1} \\ i_{AFE,2} \end{bmatrix}}_{i_{AFE}} \tag{8}$$

$$\text{with:} \begin{cases} C' = C'_{DC} \cdot \begin{bmatrix} 1 & 0 \\ 0 & 1 \end{bmatrix} \\ \\ R'^{-1}_{DCT} = \frac{1}{R'_{DCT}} \cdot \begin{bmatrix} 1 & -1 \\ -1 & 1 \end{bmatrix} \end{cases}.$$

The plant model, which was a SISO system is now a MIMO system but the transfer functions remain first order transfer functions, with a pole affected by the DC capacitance and DCT resistance values. Note that the mutual coupling is due to the presence of the DCT in the network, that introduces an R'_{DCT} term in the plant matrix $H(s)^{-1}$.

The AFE controller transfer functions $T'_{dvc}(s)$, on the other hand, can be written as:

$$i_{AFE} =$$

$$\underbrace{\frac{K_{P,DVC} \cdot s + K_{I,DVC}}{s} \cdot C_{DC,AFE} \begin{bmatrix} 1 & 0 \\ 0 & 1 \end{bmatrix}}_{T'_{dvc}(s)} \underbrace{\begin{bmatrix} v^{REF}_{dc,1} - v_{dc,1} \\ v^{REF}_{dc,2} - v_{dc,2} \end{bmatrix}}_{v^{REF}_{dc} - v_{dc}}. \tag{9}$$

With (8) and (9), the reference-to-actual DC voltage transfer function $G_{dvc}(s)$ is:

$$v_{dc} = H \cdot T'_{dvc} \cdot \left(v^{REF}_{dc} - v_{dc} \right)$$

$$= \underbrace{\left[I_2 + H \cdot T'_{dvc} \right]^{-1} \cdot H \cdot T'_{dvc}}_{G_{dvc}(s)} \cdot v^{REF}_{dc}. \tag{10}$$

The voltage to power transfer function $G_{Vdc,P}$ is:

$$P_{ac} = \underbrace{V_{DC} \cdot T'_{dvc} \cdot (I_2 - G_{dvc})}_{G_{Vdc,P}(s)} \cdot v^{REF}_{dc}. \tag{11}$$

As seen in Equation 10, compared to model I, computing the transfer functions for model II involves inverting a matrix based on H, which, when the model is scaled up to larger PDNs can represent some computational burden. Note that model II is equivalent to model I if the cross-coupling terms $H_{12}(s)$ and $H_{21}(s)$ are neglected.

In Figure 8, the step responses predicted by the model II are also drawn. Similarly to the model I, the system settling time is affected largely by the resistance but very little by the capacitance. The response times of model I and model II are very similar, with a model I that predicts a slightly faster settling time than model II. So, the model I, more simple, still models correctly the transients speed. What differentiates this model from model I is that it also includes the AFE1 DC voltage response. The initial voltage step in AFE2 also drops the voltage in AFE1. This initial voltage drop is increasing with the DCT resistance and bus capacitance.

3.2 | Modeling of the system in VR-PR configuration

The plant model remains the same as the VR-VR configuration Model II, presented mathematically in (8).

$$\begin{cases} v_{dc} = H \cdot i_{AFE} \\ H = (I_2 - H_V)^{-1} \cdot H_I \end{cases} \tag{12}$$

As AFE1 is in voltage regulation and AFE2 is in power regulation, the control loop can be sketched as in Figure 10c. The DC voltage can be written as:

$$v_{dc} = H \cdot \left(\underbrace{G_{REF} \begin{bmatrix} 0 & 0 \\ 0 & 1 \end{bmatrix}}_{G_I(s)} i^{REF}_{AFE} + \underbrace{T'_{dvc} \cdot \begin{bmatrix} 1 & 0 \\ 0 & 0 \end{bmatrix}}_{G_V(s)} \cdot (v^{REF}_{dc} - v_{dc}) \right). \tag{13}$$

And from that, the power reference to voltage transfer function $G_{P,Vdc}$ can be computed:

$$v_{dc} = (I_2 + H \cdot G_V)^{-1} \cdot G_I \cdot i^{REF}_{AFE}$$

$$= \underbrace{(I_2 + H \cdot G_V)^{-1} \cdot G_I \cdot \frac{1}{V_{DC}}}_{G_{P,Vdc}(s)} \cdot P^{REF}_{ac}. \tag{14}$$
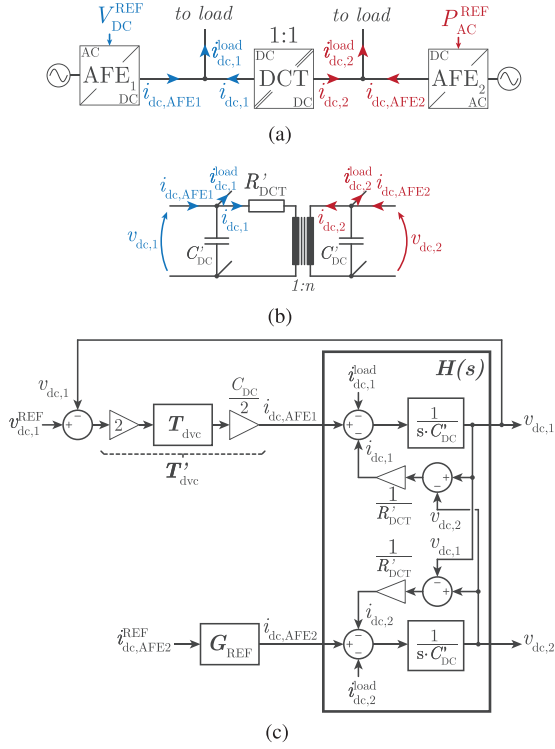
FIGURE 10 Simplified DC System in VR-PR configuration: (a) system layout, (b) equivalent circuit and (c) control loop.

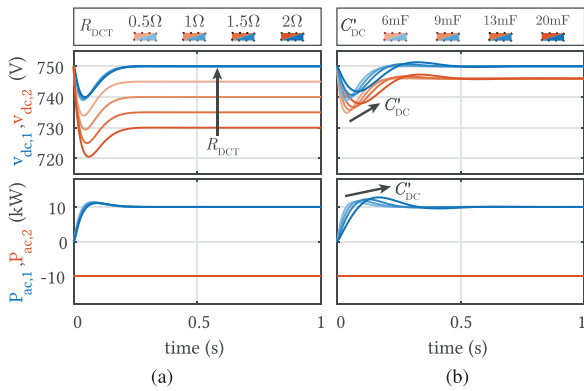**FIGURE 11** Step response to a 10 kW step for different (a) DCT resistance, (b) DCT capacitances for the PDN in VR-PR configuration.

The power transfer function $\boldsymbol{G}_{\mathrm{Pac,Pac}}(s)$ is:

$$\boldsymbol{P}_{\mathrm{ac}} = \underbrace{(\boldsymbol{I}_2 + \boldsymbol{G}_{\mathrm{V}} \cdot \boldsymbol{H})^{-1} \cdot \boldsymbol{G}_{\mathrm{I}}}_{\boldsymbol{G}_{\mathrm{Pac,Pac}}(s)} \cdot \boldsymbol{P}_{\mathrm{ac}}^{\mathrm{REF}}. \quad (15)$$

Together, $\boldsymbol{G}_{\mathrm{Pac,Pac}}(s)$ and $\boldsymbol{G}_{\mathrm{P,Vdc}}(s)$ are modeling, respectively, the voltage and power responses to power reference changes in AFE2. Based on those transfer functions, in Figure 11, response to AFE2 a 10 kW power reference step is computed for different resistance and capacitance values. Large power voltage drops are observed. The DCT resistance, mainly affecting the steady-state as the DC voltage steady-state is proportional to

the resistance, does have however very little impact on the voltage drops. On the other contrary, the capacitance reduces those drops while increasing the system response time. Compared to the VR-VR models, this large voltage drop is occurring on both DC buses, and is originated primarily from the cross-coupling of the DC buses. Therefore, a simplification like in VR-VR Model I, where the cross-coupling terms H_{12} and H_{21} are nullified cannot be considered for an accurate prediction of the system dynamics.

3.3 | Extension to larger PDNs

Using the results for the simple 2 DC bus PDNs and a similar approach, it is possible to expand the PDN model for more than two AFEs and more than one DCT.

First, the plant transfer function $\boldsymbol{H}(s)$ presented in Equation 8 becomes:

$$\underbrace{\begin{bmatrix} v_{\mathrm{dc},1} \\ ... \\ v_{\mathrm{dc},n} \end{bmatrix}}_{\boldsymbol{v}_{\mathrm{dc}}} = \underbrace{\left(\boldsymbol{C}'s + \boldsymbol{R}_{\mathrm{DCT}}'^{-1}\right)^{-1}}_{\boldsymbol{H}(s)} \cdot \underbrace{\begin{bmatrix} i_{\mathrm{AFE},1} \\ ... \\ i_{\mathrm{AFE},n} \end{bmatrix}}_{\boldsymbol{i}_{\mathrm{AFE}}}, \quad (16)$$

where n is the number of buses in the system. $\boldsymbol{C}$ is the capacitance matrix:

$$\boldsymbol{C}' = \begin{bmatrix} \ddots & & 0 \\ & C_{\mathrm{DC},i}' & \\ 0 & & \ddots \end{bmatrix}, \quad (17)$$

where $C_{\mathrm{DC},i}$ is the sum of all the capacitances connected to bus i, this may include AFEs and DCTs DC-link capacitances. $\boldsymbol{R}_{\mathrm{DCT}}^{-1}$ is the admittance matrix:

$$\boldsymbol{R}_{\mathrm{DCT}}'^{-1} = \begin{bmatrix} \ddots & & -\dfrac{1}{R_{\mathrm{DCT},ij}'} \\ & \sum_k \dfrac{1}{R_{\mathrm{DCT},ik}'} & \\ -\dfrac{1}{R_{\mathrm{DCT},ij}'} & & \ddots \end{bmatrix}, \quad (18)$$
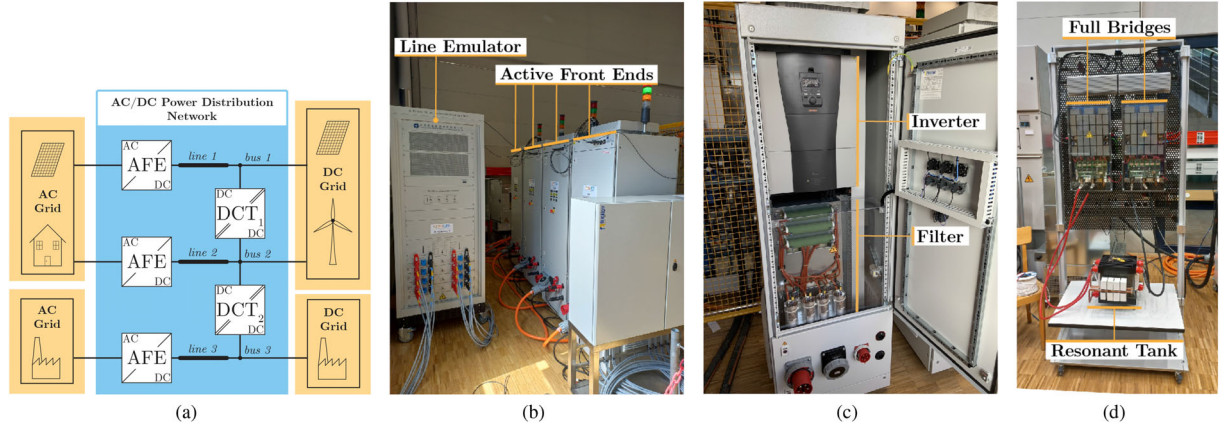
where $R_{\mathrm{DCT},ij}'$ is the resistance of the DCT connected between bus i and j.

Secondly, (13) can be adapted for a system with n_{VR} VR-AFEs and n_{PR} PR-AFEs. The new system equation would then be:

$$\boldsymbol{v}_{\mathrm{dc}} = \boldsymbol{H} \cdot \left(\boldsymbol{G}_{\mathrm{I}} \cdot \boldsymbol{i}_{\mathrm{AFE}}^{\mathrm{REF}} + \boldsymbol{G}_{\mathrm{V}} \cdot \left(\boldsymbol{v}_{\mathrm{dc}}^{\mathrm{REF}} - \boldsymbol{v}_{\mathrm{dc}}\right)\right), \quad (19)$$

with the transfer functions $\boldsymbol{G}_{\mathrm{V}}$ and $\boldsymbol{G}_{\mathrm{I}}$ rewritten as:

$$\boldsymbol{G}_{\mathrm{V}}(s) = \begin{bmatrix} \ddots & & 0 \\ & T_{\mathrm{dvc},i}' & \\ 0 & & \ddots \end{bmatrix}, \boldsymbol{G}_{\mathrm{I}}(s) = \begin{bmatrix} \ddots & & 0 \\ & G_{\mathrm{REF},i} & \\ 0 & & \ddots \end{bmatrix}, \quad (20)$$

FIGURE 12 Hybrid AC/DC distribution system considered (a) scheme, (b) four active front ends and line emulator, (c) active front end elements, (d) DC transformer.

where $T'_{\text{dvc},i}$ is the AFE i DC voltage controller transfer function and $G_{\text{REF},i}$ is the AFE i power reference transfer function.

Equivalently to the voltage and power equations for VR-VR and VR-PR configurations (equations (10), (11), (14) and (15)), based on the new system equation (19), a new set of generalized equations can be obtained:

$$
\begin{cases}
\boldsymbol{v}_{\text{dc}} = \underbrace{(\boldsymbol{I}_n + \boldsymbol{H} \cdot \boldsymbol{G}_{\text{V}})^{-1} \cdot \boldsymbol{H} \cdot \boldsymbol{G}_{\text{V}}}_{\boldsymbol{G}_{\text{dvc}}(s)} \cdot \boldsymbol{v}_{\text{dc}}^{\text{REF}} \\
\qquad + \underbrace{(\boldsymbol{I}_n + \boldsymbol{H} \cdot \boldsymbol{G}_{\text{V}})^{-1} \cdot \boldsymbol{H} \cdot \boldsymbol{G}_{\text{I}} \cdot \boldsymbol{V}_{\text{DC}}^{-1}}_{\boldsymbol{G}_{\text{P,Vdc}}(s)} \cdot \boldsymbol{P}_{\text{ac}}^{\text{REF}} \\
\boldsymbol{P}_{\text{ac}} = \underbrace{\boldsymbol{V}_{\text{DC}} \cdot \boldsymbol{G}_{\text{V}} \cdot (\boldsymbol{I}_2 - \boldsymbol{G}_{\text{dvc}})}_{\boldsymbol{G}_{\text{Vdc,P}}(s)} \cdot \boldsymbol{v}_{\text{dc}}^{\text{REF}} \\
\qquad + \underbrace{(\boldsymbol{I}_n + \boldsymbol{G}_{\text{V}} \cdot \boldsymbol{H})^{-1} \cdot \boldsymbol{G}_{\text{I}}}_{\boldsymbol{G}_{\text{Pac,Pac}}(s)} \cdot \boldsymbol{P}_{\text{ac}}^{\text{REF}}
\end{cases} . \quad (21)
$$

For any mixed VR- and PR-AFEs configuration, the transfer functions $\boldsymbol{G}_{\text{dvc}}$, $\boldsymbol{G}_{\text{P,Vdc}}$, $\boldsymbol{G}_{\text{Vdc,P}}$ and $\boldsymbol{G}_{\text{Pac,Pac}}$ can predict the system dynamics based on elements parameters. This model requires to invert a potentially large $\boldsymbol{H}$ matrix and hence, similarly to the approach followed for VR-VR Model I, the matrix can be reduced to only the direct terms H_{ii}, if all the AFEs of the system are in voltage regulation mode.

4 | EXPERIMENTAL SETUP

To validate the models developed in the previous sections, a PDN composed of three DC buses, two DCTs and three AFEs is employed as illustrated in Figure 12. The nominal DC voltage is 750 V and AC voltage is 400 Vac.

The AFE used in this study, pictured in Figure 12c are 45 kW rated with power stage parameter values described in Table 3. The controller gains for the GCC, DVC and PLL are summarized in Table 4. As seen in Figure 13a, where a VR-AFE voltage step for an unloaded DC bus is plotted, the DVC response time

TABLE 2 DCT equivalent model parameters.

$R_{\text{DCT}}^{\text{TH}}$		L_{DC}	
Param.	**Value**	**Param.**	**Value**
β^{TH}	0.97	α^{TH}	1.20
R_{total}^{MEAS}	0.46 Ω	L_{r}	11.6 μH
$R_{\text{DCT}}^{\text{TH}}$	0.43 Ω	$L_{\text{DCT}}^{\text{TH}}$	16.7 μH

TABLE 3 AFE power stage parameter values.

Parameter	Value
f_{SW}	8 kHz
L_1	600 μH
R_{L1}	66 m Ω
C	100 μF
L_2	300 μH
R_{L2}	33 m Ω
$C_{\text{DC,AFE}}$	4.7 mF

is very fast and tracks well the voltage ramp. This ramp, set at 200 V/s, is far faster than the witnessed response times (circa 1 s) when DCTs are employed. Hence, this ramp, not modeled in the model, can be neglected and the response for a stiff reference step is considered. In Figure 13b, a reactive power step is presented. This reactive power response time is also very fast, around than 30 ms, therefore, the reference transfer function G_{ref} can be approximated to a unit transfer function $G_{\text{ref}}(s) \approx 1$.
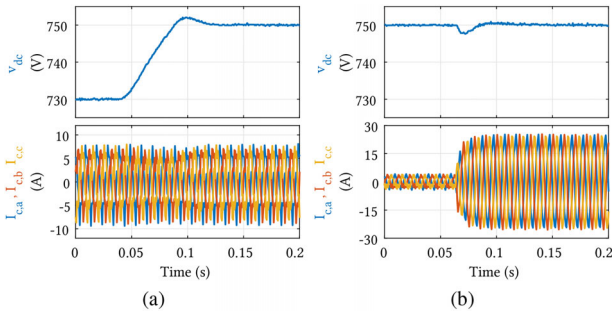
The two LLC converter-based DCTs considered in this study, with one unit pictured in Figure 12d, are rated for 50 kW and have a power stage parameter values described in Table 5.

In order to operate, several key features are added to the controller scheme in Figure 3. A power reversal method (PRM) determines the active stage to have bidirectional power trans-

TABLE 4   AFE controller gains.

Gain	Value
$K_{I,GCC}$	2.4
$K_{R,GCC}$	0.267
ω_{LPF}^{REF}	20 rad s^{-1}
$K_{P,DVC}$	133
$K_{I,DVC}$	2133
$(\frac{dv}{dt})_{max}$	200 V s^{-1}
$K_{P,PLL}$	92
$K_{I,PLL}$	4232

FIGURE 14   DCT operation with two DC voltage sources (a) DC voltage step from 750 V to 760 V. (b) Branch current and resonant curves at 20 kW.
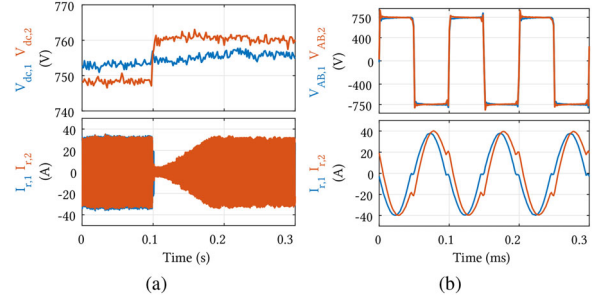

FIGURE 13   VR-AFE operation with unloaded DC bus (a) DC voltage step from 730 V to 750 V. (b) Reactive power step from 0 kVAr to 10 kVar.

TABLE 5   DCT power stage parameter values.

Parameter	Value
f_{SW}	10 kHz
C_r	37.5 μF
L_r	11.6 μH
L_m	750 μH
f_r	10.7 kH
n	1
$C_{DC,DCT}$	1.02 mF

5 | MODEL VALIDATION

## 5.1 | VR-VR and VR-PR model validation

In Figure 15a, experimental voltage and power step response of the PDN in the VR-VR configuration are compared to the models I and II responses. The models responses are very similar to the experimental response with a settling time of around 1 s for the two models and the experiments. Compared to the experiments, the model I overestimates the voltage and power response (slightly lower settling time) while the model II underestimates it (slightly higher settling time).

The model II models accurately the initial voltage drop for both AFEs (AFE1: experimentally voltage drop of 5 V compared to 7 V in model II, AFE2: experimentally drop of 13 V compared to 10 V in model II), whereas instead, the model I fails to accurately model the initial voltage drop for AFE2: only 4 V instead of 10 V. In Figure 15b, the model derived for the VR-PR configuration is compared to the experimental results showing strong correlation between the two steps responses. The initial voltage drops in the DC buses 1 and 2 is well estimated.

These results validate the model capability to predict accurately power and voltage transients.

5.2 | DC line effect

$$C' = \begin{bmatrix} C_{DC,AFE} + C_{DC,DCT} & 0 & 0 \\ 0 & C_{DC,AFE} + 2 \cdot C_{DC,DCT} & 0 \\ 0 & 0 & C_{DC,AFE} + C_{DC,DCT} \end{bmatrix}, \; R'^{-1}_{DCT} = \frac{1}{R_{DCT}} \cdot \begin{bmatrix} 1 & -1 & 0 \\ -1 & 2 & -1 \\ 0 & -1 & 1 \end{bmatrix}, \; G_V(s) = T'_{dvc} \cdot \begin{bmatrix} 1 & 0 & 0 \\ 0 & 1 & 0 \\ 0 & 0 & 1 \end{bmatrix} \quad (22)$$

fer [20, 21] by comparing the DC bus voltages. An idle mode (IdM) detection method is deployed to limit the losses when no load is connected and an overcurrent limiter (OL) [22] can limit the power when high powers are being processed. Finally, a soft-start (SS) method protects the system against inrush currents [20]. DCT operation with two DC voltage sources (DC power supplies) is demonstrated in Figure 14.

The theoretical and experimental DC resistance and inductances are then computed and given in Table 2 using (3).

Voltage and power steps are repeated with the two PDN configurations for different DC lines, emulated by the line emulator presented in Figure 12b. The line emulator reproduces DC lines, modeled as a lumped π-section, for lengths presented in Table 6. As the capacitances of the lines are small compared to the DCT and AFE DC-link capacitances, the models derived in the previous sections, that ignored those capacitances, are still valid. Lines are connected on each side of the DCT to achieve a
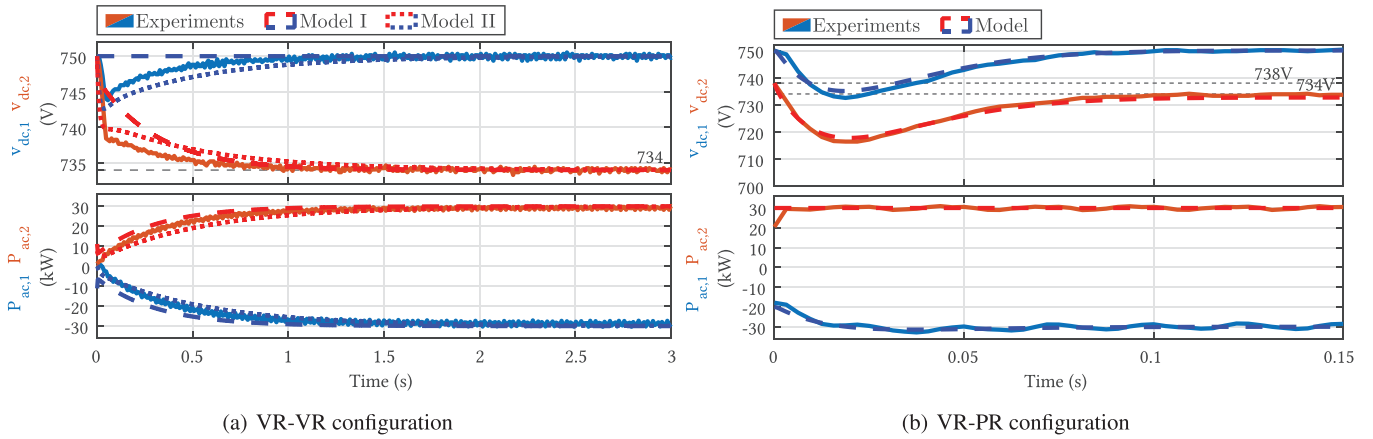
FIGURE 15 Comparison of experimental and modeled power step responses. (a) VR-VR configuration for a voltage reference step in AFE2 (750 V to 734 V). (b) VR-PR configuration for a power reference step in AFE2 (20 kW to 30 kW, with a non-filtered step of power reference ($G_{REF}(s) = 1$)).

defined total DC line length and the selected line lengths for the experimental evaluation are summarized in Table 7.

In the VR-VR configuration, the resulting step response waveforms are plotted in Figure 16a. As the line length increases, the overall grid resistance increases and, naturally, for an identical voltage step, the steady-state power decreases. The settling time is also decreasing with the line length increase, going from 0.8 s to 0.35 s. This is coherent with the model, that predicts that the response time drops with the resistance increase.

As for the response of the system in VR-PR configuration, plotted in Figure 16b, neither the response time nor the voltage drop magnitude vary with the length. This was well predicted by the model in Figure 11, where resistance changes did not affect the response. Only the steady-state voltage decreases with the line length increase, caused naturally by the increase in total resistance R_{12}, detailed in Table 7.

TABLE 6 Line emulator line length and π-section values.

l	R_l	L_l	C_l
250 m	40 mΩ	140 μH	35 μF
500 m	80 mΩ	280 μH	75 μF
1 km	160 mΩ	280 μH	145 μF
2 km	320 mΩ	1120 μH	290 μF

TABLE 7 Line lengths and values for the experiments.

Test	l_1	l_2	l_{total}	R_{12}	P_{AC*}
①	250 m	0 m	250 m	630 mΩ	9.52 kW
②	250 m	500 m	750 m	670 mΩ	8.95 kW
③	2 km	0 m	2 km	910 mΩ	6.59 kW
④	2 km	1 km	3 km	1070 mΩ	5.61 kW

Note 1: R_{12} is the sum of the line resistances $2 \cdot R_{l1}$, $2 \cdot R_{l2}$ and the DCT resistance R_{12}^{eq}(10 kW), from Test ① results.
Note 2: P_{ac} is the power at steady-state for the Test ① voltage step, considering R_l.

5.3 | Validation of the extended model

In Figure 12, the setup is made of three DC buses interconnected by two DCTs. In Figure 17, the setup is configured with three VR-AFEs ($n_{VR} = 3$) and two voltage steps are performed on buses 2 and 3. The response is compared with the one predicted by the extended model derived in Section 3.3. In the two tests, the model and the experimental waveforms have a very similar response, with a settling time of around 3 s and the same initial voltage drop magnitude, therefore validating the extended system model.

The model extension is validated with experiments for a larger system in VR-VR configuration ($n_{PR} = 0$) of size $n = 3$, with $n_{VR} = 3$ VR-AFEs and two DCTs as shown in Figure 17. The AFEs are identical to the AFE of Figure 12c (same ratings, same hardware values, same controller gains) and the two DCTs have similar characteristics (R_{DCT}, $C_{DC,DCT}$) as the DCT of Figure 12d.

The model responses are based on the transfer functions $G_{dvc}(s)$ and $G_{Vdc,P}(s)$ whose expressions can be found in (21) and $H(s)$ is computed via (16) using the expressions of R'^{-1}_{DCT} and C' provided in (22).

6 | IMPACT OF THE DCT ON THE SYSTEM DYNAMICS

In Figure 18, steps of AFE2 references are performed, while the AFE1 reference is maintained at 750 V. Reference steps are selected so that the power in AFE2 reaches 10 kW to 30 kW at steady-state. Voltage and power values can be found in Table 8.

When the PDN is set in VR-VR configuration, voltage and power response waveforms for a voltage step in AFE2 are shown in Figure 18a. The voltage and power settling time is varying between 0.78 s and 1.10 s. Furthermore, at steady-state, the voltage difference between DC buses 1 and 2 is not proportional to the power. This implies that the equivalent resistance

TABLE 8 Power and voltage steps for schemes comparison.

Test	$V_{dc,1}$	$V_{dc,2}^{ini} \to V_{dc,2}^{fin}$	$P_{ac,2}^{ini} \to P_{ac,2}^{fin}$	R_{12}^{eq}
⑤	750 V	750 V → 742 V	0 kW → 10 kW	0.59 Ω
⑥	750 V	750 V → 737 V	0 kW → 20 kW	0.46 Ω
⑦	750 V	750 V → 734 V	0 kW → 30 kW	0.40 Ω

Note: $R_{12}^{eq} = \dfrac{V_{dc,1} \cdot (V_{dc,1} - V_{dc,2}^{fin})}{P_{ac,2}^{fin}}$.

between the two buses R_{12}^{eq} (therefore the DCT resistance R_{DCT}') is varying with power. Values for the different powers points are summarized in Table 8. Similar conclusion can be drawn from Figure 18b, where, for the VR-PR configuration, power steps are performed and the voltage settling time.

Therefore, for an accurate prediction of the PDN behavior, the DCT resistance variation must be taken into account. Also, the theoretical value R_{DCT}^{TH} of 0.4 Ω computed in Table 2 is only valid for at high powers.

6.1 | Effect of power reversal

In Figure 19, 10 kW power steps from 0 kW to 30 kW are performed. As predicted by the model, the voltage drop should remain constant as the power step is the same and the DCT resistance (only parameter affected by the power setpoint) is not changed. This voltage drop is indeed constant for 10 kW→20 kW and 20 kW→30 kW (around 17 V). However, for the 0 kW→ 10 kW test, the voltage drop at 0 kW is significantly larger (around 22 V). One thing that is noticed is the power flow reversal event, and the voltage curve shape that differ between this test and the other power steps.

Power reversal in DCT is detected by a power reversal method as presented in Section 4. According to the PRM, the active power stage is first switched off and, after a blanking time, the passive power stage is then activated. During this blanking time, the DCT is not active and as seen in Figures 19, 21, the delay caused by the detection time and the blanking time
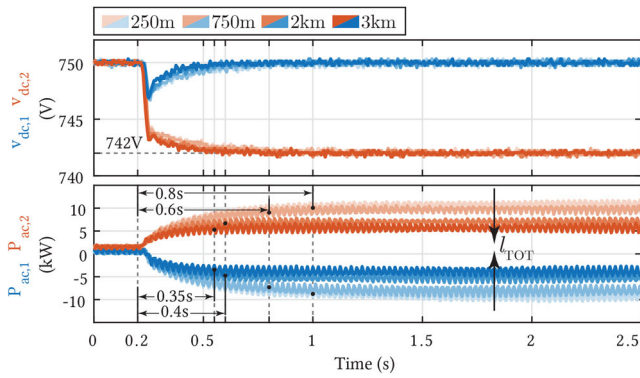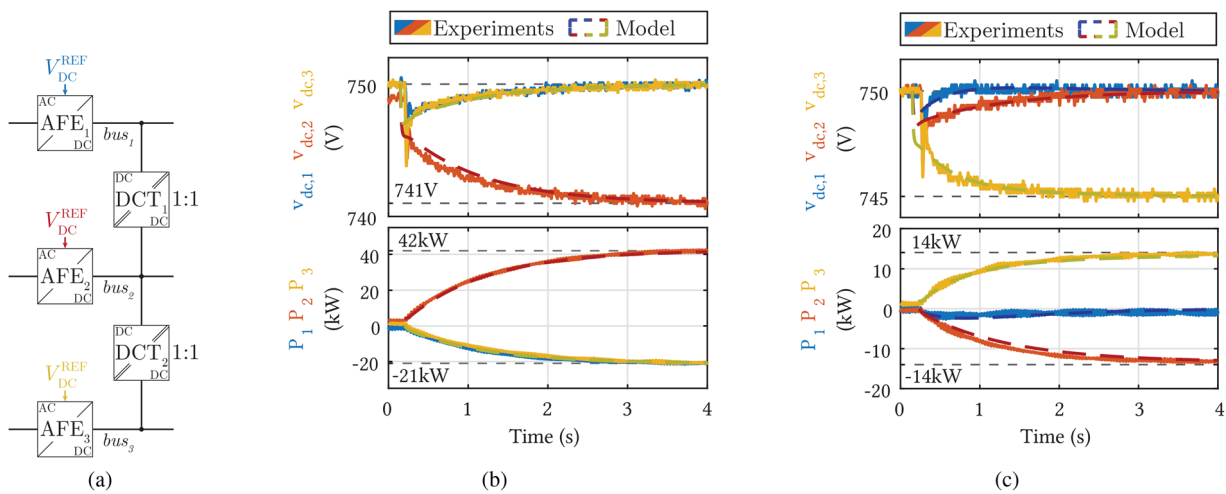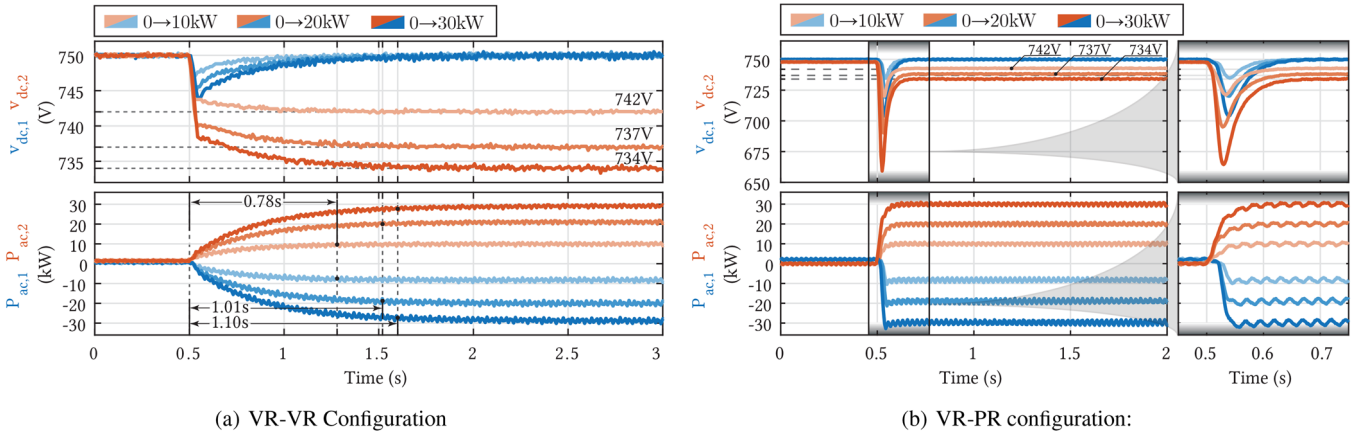

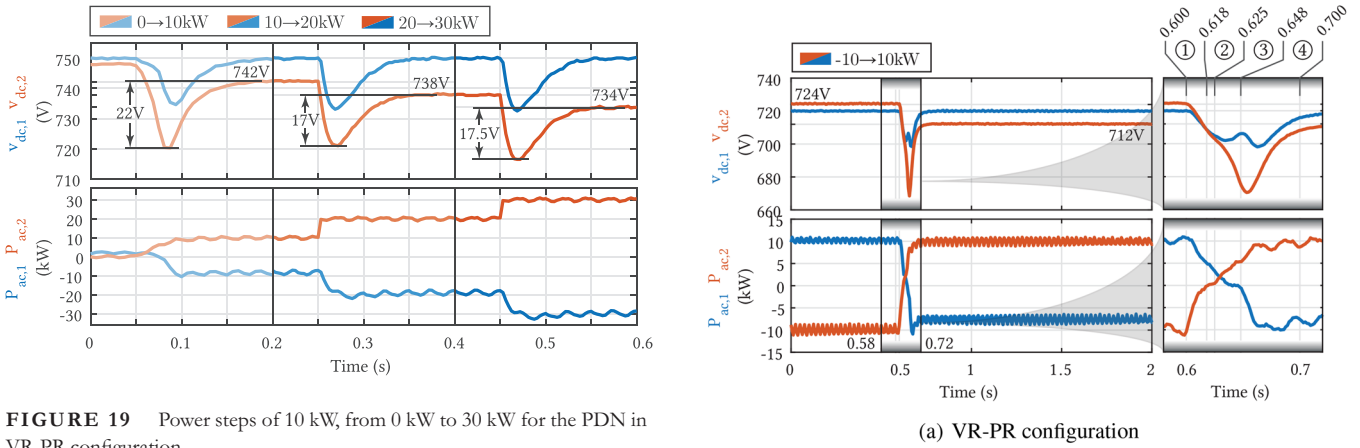(a) VR-VR configuration
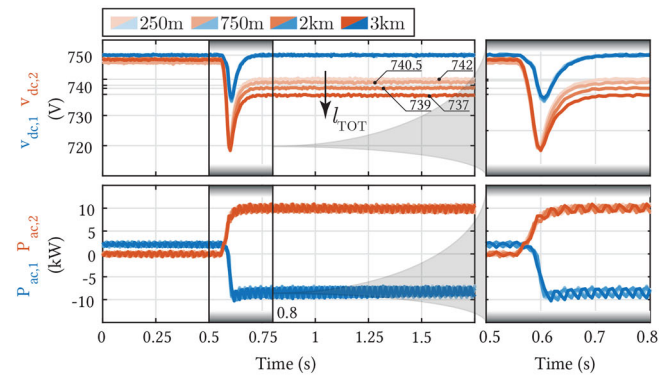
(b) VR-PR configuration

FIGURE 16 Voltage and power steps for different DC line lengths (a) VR-VR configuration: voltage step of AFE2 from 750 V to 742 V. (b) VR-PR configuration: power steps of AFE2 from 0 kW to 10 kW.

(a)   (b)   (c)

FIGURE 17 Step response to voltage steps in a three bus system (a) scheme with three AFEs and two DCTs, step response to a voltage reference step for (b) AFE2 (750–741 V), (c) AFE3 (750–V).

FIGURE 18 Power steps of Tests ①, ② and ③: (a) VR-VR configuration: voltage steps of AFE2 from 750 V to 742 V, 737 V, 734 V and (b) VR-PR configuration: power steps of AFE2 from 0 kW to 10 kW, 20 kW, 30 kW.


FIGURE 19 Power steps of 10 kW, from 0 kW to 30 kW for the PDN in VR-PR configuration.

may lead to significant voltage drop that must hence be quantified. The power reversal method of the DCT is based on the DCT input voltages difference and when the voltage difference exceeds 3V, the active full-bridge is de-activated and after 25 ms, the other full-bridge is activated.

6.1.1 | VR-PR configuration

In Figure 20, a power reversal test is performed with the system in VR-PR configuration. When looking at the power transition period, a large voltage drop of 42 V can be observed in the DC bus 2 voltage $V_{dc,2}$ along with a voltage fluctuation in the DC bus 1 voltage $V_{dc,1}$ as the power flow reverses direction.

The effect of the DCT power reversal action can be detailed in Figure 20. The sequence of actions is described in Figure 20b. First, in the [0.6 s, 0.618 s] time interval, the AC power in both AFE1 and AFE2 drops. As the DC voltage difference reaches 0 V, the power across the DCT is null. In this second period (time interval [0.618 s, 0.625 s]), the power cannot flow through the DCT as the Full-Bridge FB_1, not switching, blocks the current. In a third period (time interval [0.625 s, 0.648 s]), the power reversal algorithm detects the voltage difference and dis-

(a) VR-PR configuration

(b)
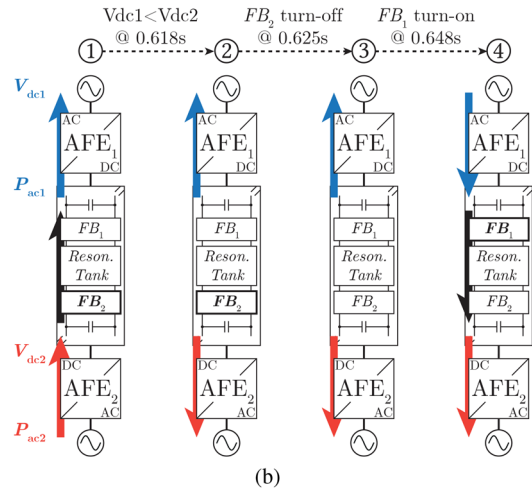
FIGURE 20 PDN in VR-PR configuration, power step from −10 kW to 10 kW (a) voltage and power response and (b) power reversal sequence.

ables FB_1. Yet, during those two periods (i.e. the whole time interval [0.618 s, 0.648 s]), the AFE2 power increases, taking energy from the capacitances $C_{DC,AFE2}$ and $C_{DC,DCT}$ leading to a large voltage drop in $V_{dc,2}$. In the meantime, the DC voltage $V_{dc,1}$ increases by the action of the AFE DC voltage controller.
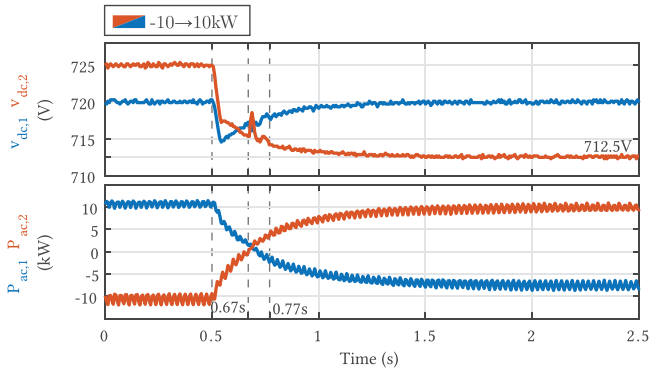
FIGURE 21   PDN in VR-VR configuration, power step from −10 kW to 10 kW.

After a blanking time, in a fourth period (time interval [0.648 s, 0.700 s]), the full bridge FB_2 is activated and the power flow from side 1 to side 2 of the DCT is enabled. During the first 10 ms, the power is first limited by the slow start (SS) function of DCT.

The voltage drop depends hence mainly on the total line capacitance value C'_{DC} and on the DCT power reversal method-induced blanking time as, during this period, the capacitance is discharged or charged, by the action of the power-regulating AFE. The line resistance does not play a noticeable role in the voltage discharge during the power reversal blanking period and this is why in Figure 16b, the large voltage drop in $V_{dc,2}$ remains relatively constant for various line lengths.

6.1.2 | VR-VR configuration

In Figure 21, the power reversal test of −10 kW→10 kW is performed for the VR-VR configuration. As it can be observed, the power and DC voltage dynamics is not much changed as both VR-AFEs regulate the DC bus voltage. Therefore, during the power reversal blanking time, between 0.67 s and 0.77 s, the DC voltages are properly regulated and no particular voltage drop occurs.

7 | CONCLUSION

The use of resonant, open-loop operated, DC transformers in a power distribution network introduces a new degree of freedom for the active front end control. In DC buses interconnected by resonant, open-loop controlled DCTs, AFEs can be set in various mixes of voltage regulating AFEs (VR-AFEs) and power regulating AFEs (PR-AFEs) to enable the power flow and voltage regulation across the network. This paper has analyzed the impact of the DCT on the power and voltage dynamic performances of a power distribution network under different AFE configurations.

A summary of the qualitative performances of the different AFE configurations is presented in Table 9. When using VR-AFEs only, the system power flow and voltage response

TABLE 9   Comparison of the PDN dynamics using VR-VR or VR-PR configurations.

	VR-VR configuration	VR-PR configuration
Settling time	Short	Long
Voltage overshoot/undershoot	No	High
Impact of DC line length	Strong	Weak
Impact of DCT resistance	Strong	Weak

time is slowed down compared to the potential VR-AFE response time, while for mixed VR- and PR-AFEs configurations, where the PR-AFEs are controlling the power flows, the power response is much faster but at the expense of large voltage spikes. The dynamics of the configuration with only VR-AFEs is mainly affected by the DCT equivalent resistance R'_{DCT}: the larger it is, the smaller the response time is. In the meantime, the mixed VR/PR-AFEs configuration is not affected by the DC line resistance but larger DC capacitances can reduce the voltage spikes.

A parametric model that can predict very well the network transients has been developed and verified experimentally. The model can be easily set knowing the network topology, the AFE controllers transfer functions and the DC buses equivalent capacitances and equivalent resistances.

As seen experimentally, the DCT parameters play a large role in the network dynamic response and the model predicts well the dynamics when the parameters are constant. Among them, the resistance of the DCT is a crucial element for the estimation but it strongly depends on both the design (e.g. resonant tank, switching frequency) and the operating condition (e.g. the power transmitted). This work focused on a specific DCT design, but explicitly considered the effect of the change of operating point on the equivalent DC resistance. It is hence important to take the steady-state power conditions into consideration to properly model the PDN dynamic response. Furthermore, bidirectional power flow is possible with the use of a power reversal method (PRM). This method however introduces a blanking time, where no power is being transferred through the DCT, causing significant voltage drops in the connected DC buses, especially when PR-AFEs are controlling the power flows, stressing out the importance of having PR methods introducing blanking times as small as possible.

This paper has stressed the impact of DCTs in AC/DC distribution networks where power and voltages are regulated with AFEs. AFEs should be set in voltage regulating configurations when slow dynamics is not a constraint and voltage spikes and drops must be avoided. Models proposed in this paper accurately estimated power and voltage transients during power and voltage steps. AFEs should be set in power regulating configurations when fast transients are desired and when voltage drops or spikes are acceptable. It could then be used to size the elements (converter controllers, DC-link capacitances…) or do grid planning, as the power transients can be predicted.

AUTHOR CONTRIBUTIONS

Jules Mace: Writing - review and editing. Renan Pillon Barcelos: Writing - review and editing. Max Dupont: Writing - review and editing. Andrea Cervone: Writing - review and editing. Drazen Dujic: Writing - review and editing.

CONFLICT OF INTEREST STATEMENT

The authors declare no conflicts of interest.

DATA AVAILABILITY STATEMENT

The data that support the findings of this study are available from the corresponding author upon reasonable request.

ORCID

Jules Mace https://orcid.org/0000-0002-2951-0480
Andrea Cervone https://orcid.org/0000-0003-1865-892X

REFERENCES

1. Liu, X., Wang, P., Loh, P.C.: A Hybrid AC/DC Microgrid and Its Coordination Control. IEEE Trans. Smart Grid 2(2), 278–286 (2011)
2. Hofer, J., Svetozarevic, B., Schlueter, A.: Hybrid AC/DC building microgrid for solar PV and battery storage integration. In: 2017 IEEE Second International Conference on DC Microgrids (ICDCM), pp. 188–191. IEEE, Piscataway (2017)
3. Ambia, M.N., Al-Durra, A., Muyeen, S.M.: Centralized power control strategy for AC-DC hybrid micro-grid system using multi-converter scheme. In: IECON 2011-37th Annual Conference of the IEEE Industrial Electronics Society, pp. 843–848. IEEE, Piscataway (2011). iSSN: 1553-572X
4. Huang, J., Xiao, J., Wen, C., Wang, P., Zhang, A.: Implementation of bidirectional resonant DC transformer in Hybrid AC/DC micro-grid. IEEE Trans. Smart Grid 10(2), 1532–1542 (2019)
5. Huang, J., Zhang, X., Zhang, T.: Transmission power analysis and control of the DC transformer in hybrid AC/DC microgrid. In: 2018 International Power Electronics Conference (IPEC-Niigata 2018 -ECCE Asia), pp. 2980–2985. IEEE, Piscataway (2018)
6. Dujic, D., Zhao, C., Mester, A., Steinke, J.K., Weiss, M., Lewdeni.Schmid, S., et al.: Power electronic traction transformer-low voltage prototype. IEEE Trans. Power Electron. 28(12), 5522–5534 (2013)
7. Zhao, T., Yang, L., Wang, J., Huang, A.Q.: 270 kVA solid state transformer based on 10 kV SiC power devices. In: 2007 IEEE Electric Ship Technologies Symposium, pp. 145–149. IEEE, Piscataway (2007)
8. Beiranvand, H., Hoffmann, F., Pascal, Y., Hahn, F., Liserre, M.: Multiwinding transformer leakage inductance optimization for power flow decoupling in multiport DC-DC converters. In: 2021 IEEE 15th International Conference on Compatibility, Power Electronics and Power Engineering (CPE-POWERENG), pp. 1–8. IEEE, Piscataway (2021)
9. Zhou, K., Jin, Q., Lan, Z., Tu, C., Guo, M., Liu, G.: The study of power electronic transformer on power flow control and voltage regulation in DC micro-grid. In: 2015 5th International Conference on Electric Utility Deregulation and Restructuring and Power Technologies (DRPT), pp. 2166–2172. IEEE, Piscataway (2015)
10. Huang, L., Zong, C., Yang, X., Chen, W., Zhu, Y., Bi, K.: Power flow calculation of distribution network with multiple energy routers. IEEE Access 9, 23489–23497 (2021)
11. Liu, B., Wu, W., Zhou, C., Mao, C., Wang, D., Duan, Q., et al.: An AC-DC hybrid multi-port energy router with coordinated control and energy management strategies. IEEE Access 7, 109069–109082 (2019)
12. Kaifang, Z., Li, Z., Tan, L., Renliang, C.: New energy access technology based on simultaneous AC and DC distribution network. In: 2017 Chinese Automation Congress (CAC), pp. 5377–5381. IEEE, Piscataway (2017)
13. Li, X., Guo, L., Li, Y., Hong, C., Zhang, Y., Guo, Z., et al.: Flexible interlinking and coordinated power control of multiple DC microgrids clusters. IEEE Trans. Sustain. Energy 9(2), 904–915 (2018)
14. Wang, X., Peng, Y., Weng, C., Xia, Y., Wei, W., Yu, M.: Decentralized and per-unit primary control framework for DC distribution networks with multiple voltage levels. IEEE Trans. Smart Grid 11(5), 3993–4004 (2020)
15. Gao, S., Jia, H., Marnay, C.: Techno-economic evaluation of mixed AC and DC power distribution network for integrating large-scale photovoltaic power generation. IEEE Access 7, 105019–105029 (2019)
16. Huber, J.E., Miniböck, J., Kolar, J.W.: Generic derivation of dynamic model for half-cycle DCM series resonant converters. IEEE Trans. Power Electron. 33(1), 4–7 (2018)
17. Huang, J., Zhang, X., Mao, T.: Multitime scale frequency regulation of a general resonant DC transformer in a hybrid AC/DC microgrid. IEEE Trans. Ind. Electron. 68(10), 9641–9651 (2021)
18. Barcelos, R.P., Dujić, D.: Direct current transformer impact on the DC power distribution networks. IEEE Trans. Smart Grid 13(4), 2547–2556 (2022)
19. Suntio, T., Messo, T., Puukko, J.: Power electronic converters dynamics and control in conventional and renewable energy applications, 1st ed. Wiley-VCH Verlag GmbH & Co. KGaA, Weinheim (2018)
20. Jung, J.H., Kim, H.S., Ryu, M.H., Baek, J.W.: Design methodology of bidirectional CLLC resonant converter for high-frequency isolation of DC distribution systems. IEEE Trans. Power Electron. 28(4), 1741–1755 (2013)
21. Barcelos, R.P., Kucka, J., Dujic, D.: Power reversal algorithm for resonant direct current transformers for DC networks. IEEE Access 10, 127117–127127 (2022)
22. Kucka, J., Dujic, D.: Current limiting in overload conditions of an LLC-converter-based DC transformer. IEEE Trans. Power Electron. 36(9), 10660–10672 (2021)